Two Level Simulation of High-Re Wall-Bounded Flows and Isotropic Turbulence

K. A. Kemenov [*]   A. G. Gungor[*]

S. Menon[†]

School of Aerospace Engineering, Georgia Institute of Technology, Atlanta, Georgia 30332-0150

Two level simulation (TLS) is a novel approach, which is based on the decomposition of velocity into large-scale and small-scale components, has been applied to simulate near-wall and isotropic turbulence. A coupled system of equations that is not based on an eddy-viscosity type of assumption uses an explicit reconstruction of the small-scale velocity field. The small-scale equations are modeled on a family of three one-dimensional, orthogonal lines that are embedded inside the three-dimensional large-scale grid. Results suggest that the baseline TLS approach can capture important features of high-Re turbulent flows using relatively coarse grids.

I.   Introduction

Direct numerical simulation (DNS) of high Reynolds (Re) number wall-bounded flows is computationally very expensive because of the resolution requirement in the near-wall region. Even with the advent of massively parallel supercomputers, DNS is still limited to low-Re number flows[1] ($Re_\tau = 590$). Recently, large eddy simulation (LES) has become a viable method to study high-Re complex flows. However, past LES of high-Re wall-bounded flows have not proven successful in capturing the near-wall dynamics, which is dominated by quasi-streamwise vortices, unless DNS like resolution is employed near the wall. This has led to methods in which only the outer layer is computed while the near-wall region is modeled. Many near-wall subgrid models have been proposed,[2] but so far such models have shown a relatively limited success. A fundamental limitation is that most models employ empirical arguments about small-scale isotropy and requires the introduction of arbitrary model parameters. However, the near-wall region is strongly anisotropic and to resolve it near-DNS resolution has been required. This resolution need is prohibitive for high-Re flows and thus, new methods are needed that are not dependent on DNS resolution near the wall.

The present approach, called two level simulation (TLS), departs significantly from LES and is similar to several alternative approaches (referred loosely here as "decomposition" approaches) that have emerged in literature recently. In contrast to LES, where decomposition is introduced through spatial filtering and the major effort is concentrated on the subgrid-scale stress (SGS) modeling, in "decomposition" approaches considerable attention is devoted to modeling of small-scale velocity itself. This usually involves a derivation of the governing equation for small-scale velocity with its subsequent simplification based on some physical arguments.[3,4] In TLS, the small-scale velocity field is explicitly reconstructed by solving approximate small-scale equations on a family of 1D grid lines embedded inside the 3D resolved grid. The 3D small-scale velocity field constructed from these 1D lines serves as a closure for the 3D large-scale equations. The reduction in dimensionality for the small-scale equations allows the coupled TLS approach to be computationally feasible (on massively parallel machines). In this paper, we first highlight the derivation of the governing equations for large and small scales, then we discuss application of the TLS approach to the turbulent channel flow and isotropic turbulence.

---

[*]Graduate Research Assistant.

[†]Professor, AIAA Associate Fellow.

II.   Mathematical Formulation

We split velocity and pressure fields into large-scale (LS, superscript L) and small-scale (SS, superscript S) components:

$$u_i(\bar{x}, t) = u_i^L(\bar{x}, t) + u_i^S(\bar{x}, t), \quad p(\bar{x}, t) = p^L(\bar{x}, t) + p^S(\bar{x}, t) \tag{1}$$

and substitute into the incompressible Navier-Stokes equations to obtain the baseline TLS equations:

$$\frac{\partial}{\partial t}(u_i^L + u_i^S) + \frac{\partial}{\partial x_j}(u_i^L + u_i^S)(u_j^L + u_j^S) = -\frac{\partial}{\partial x_i}(p^L + p^S) + \nu\frac{\partial^2}{\partial x_j^2}(u_i^L + u_i^S) \tag{2}$$

$$\frac{\partial}{\partial x_i}(u_i^L + u_i^S) = 0 \tag{3}$$

If the SS fields (u_i^S, p^S) are known, the LS fields (u_i^L, p^L) can be determined by integrating Eqs. (2, 3). The LS velocity represents not only the filtered quantity with respect to some spatial filter (as in LES) but also any LS velocity that can be defined based on its values at the LS grid points. Once the LS quantity is defined any SS quantity is defined based on decomposition similar to Eq. (1). Rearranging Eq. (2) results in the coupled LS and SS equations:

$$\frac{\partial u_i^L}{\partial t} + \frac{\partial}{\partial x_j}(u_i^L + u_i^S)(u_j^L + u_j^S) = -\frac{\partial p^L}{\partial x_i} + \nu\frac{\partial^2 u_i^L}{\partial x_j^2} + F_i^S(u_i^S, p^S) \tag{4}$$

$$\frac{\partial u_i^S}{\partial t} + \frac{\partial}{\partial x_j}(u_i^L + u_i^S)(u_j^L + u_j^S) = -\frac{\partial p^S}{\partial x_i} + \nu\frac{\partial^2 u_i^S}{\partial x_j^2} + F_i^L(u_i^L, p^L) \tag{5}$$

The LS and SS velocities affect each other through the forcing terms F_i^S, F_i^L:

$$F_i^L(u_i^L, p^L) = -\frac{\partial u_i^L}{\partial t} - \frac{\partial p^L}{\partial x_i} + \nu\frac{\partial^2 u_i^L}{\partial x_j^2} \tag{6}$$

$$F_i^S(u_i^S, p^S) = -\frac{\partial u_i^S}{\partial t} - \frac{\partial p^S}{\partial x_i} + \nu\frac{\partial^2 u_i^S}{\partial x_j^2} \tag{7}$$

Note that all Eqs. (2, 4-5) are different forms of the full Navier-Stokes equations written for different unknown velocities, and most importantly, they do not involve any type of LES spatial filtering. Thus, the TLS formulation is inherently free from problems associated with filtering such as commutativity between filtering and differentiation, which is an issue in LES formalism near boundaries and on non-uniform grids.[5]

The last two forms of the TLS equations can be re-written in different equivalent form to highlight their connection to LES equations. Similar to velocity and pressure any quantity can be decomposed into large-scale and small-scale components. Splitting the non-linear term on the left hand side of the equations (4,5) into large and small-scale components produces the following set of the LS and SS equations:

$$\frac{\partial u_i^L}{\partial t} + \left[\frac{\partial}{\partial x_j}(u_i^L + u_i^S)(u_j^L + u_j^S)\right]^L = -\frac{\partial p^L}{\partial x_i} + \nu\frac{\partial^2 u_i^L}{\partial x_j^2} + G_i^S(u_i^L, u_i^S, p^S) \tag{8}$$

$$\frac{\partial u_i^S}{\partial t} + \left[\frac{\partial}{\partial x_j}(u_i^L + u_i^S)(u_j^L + u_j^S)\right]^S = -\frac{\partial p^S}{\partial x_i} + \nu\frac{\partial^2 u_i^S}{\partial x_j^2} + G_i^L(u_i^L, u_i^S, p^L) \tag{9}$$

Now the large and small-scale forcing terms G_i^S, G_i^L on the right hand side of the equations are given by:

$$G_i^L(u_i^L, u_i^S, p^L) = F_i^L(u_i^L, p^L) - \left[\frac{\partial}{\partial x_j}(u_i^L + u_i^S)(u_j^L + u_j^S)\right]^L \tag{10}$$

$$G_i^S(u_i^L, u_i^S, p^S) = F_i^S(u_i^S, p^S) - \left[\frac{\partial}{\partial x_j}(u_i^L + u_i^S)(u_j^L + u_j^S)\right]^S \tag{11}$$

and both Eqs. (8, 9) are equivalent to the original Navier-Stokes equations (2) written as:

$$G_i^L(u_i^L, u_i^S, p^L) + G_i^S(u_i^L, u_i^S, p^S) = 0 \tag{12}$$

In particular, this equation holds when each large-scale and small-scale parts are equal to zero simultaneously:

$$G_i^L(u_i^L, u_i^S, p^L) = 0, \quad G_i^S(u_i^L, u_i^S, p^S) = 0 \tag{13}$$

It is clear, from Eqs. (8, 9), that the former equation recover LES equation for (u_i^L, p^L) and the latter is, in fact, the small-scale equation for (u_i^S, p^S):

$$\frac{\partial u_i^L}{\partial t} + \left[\frac{\partial}{\partial x_j}(u_i^L + u_i^S)(u_j^L + u_j^S)\right]^L = -\frac{\partial p^L}{\partial x_i} + \nu \frac{\partial^2 u_i^L}{\partial x_j^2} \tag{14}$$

$$\frac{\partial u_i^S}{\partial t} + \left[\frac{\partial}{\partial x_j}(u_i^L + u_i^S)(u_j^L + u_j^S)\right]^S = -\frac{\partial p^S}{\partial x_i} + \nu \frac{\partial^2 u_i^S}{\partial x_j^2} \tag{15}$$

The requirement why Eq. (13) should hold follows from consideration of Eq. (9). It is seen that if G_i^L had not been identical zero then solution u_i^S would have had large-scale modes and would not have been small for large wave numbers, which contradicts the definition of the small-scale velocity. Similar arguments can be also applied to Eq. (8) to see that G_i^S is in fact, zero too. As a result the forcing terms F_i^S, F_i^L in the LS and the SS equations can also be written in alternative form, Eqs. (10, 11) give:

$$F_i^L(u_i^L, p^L) = \left[\frac{\partial}{\partial x_j}(u_i^L + u_i^S)(u_j^L + u_j^S)\right]^L \tag{16}$$

$$F_i^S(u_i^S, p^S) = \left[\frac{\partial}{\partial x_j}(u_i^L + u_i^S)(u_j^L + u_j^S)\right]^S \tag{17}$$

Similar scale separation applied to Eq. (3) produces the LS and SS continuity equations:

$$\frac{\partial u_i^L}{\partial x_i} = 0, \quad \frac{\partial u_i^S}{\partial x_i} = 0 \tag{18}$$

It is seen that both the LS and the SS equations are "symmetric" with respect to interchange of superscripts L and S. If one field (LS or SS) is known the other one (SS or LS) can be found by integrating corresponding governing equations. The nonlinear convective term of (15) represents the SS part of the total convective term, and can be further re-written in more convenient form. Subtracting (16) from (15) gives the final form of the SS momentum equation:

$$\frac{\partial u_i^S}{\partial t} + \frac{\partial}{\partial x_j}(u_i^L + u_i^S)(u_j^L + u_j^S) = -\frac{\partial p^S}{\partial x_i} + \nu \frac{\partial^2 u_i^S}{\partial x_j^2} + F_i^L \tag{19}$$

Finally, the coupled system of (14) and (19) along with (18) supplied by appropriate initial and boundary conditions completely defines evolution of the LS and the SS fields.

III.   Modeling of Small-Scale Governing Equation

Numerical simulation of the SS equation (19) is quite a challenge computationally since it would require resolution of the smallest scales of the flow and therefore similar to DNS. On the other hand, the LS equation (14) is solved on the coarse 3D LS grid and with a time step comparable to the characteristic turnover time of the smallest resolvable LS eddy. Therefore, the complete knowledge of the SS field in space and time may not be necessary since to close (14) one would need to know the affect of the SS fields on the LS grid at the LS times. Since the SS field evolves on a much faster time scale than the LS field we introduce two time coordinates such that:

$$u_i(\bar{x}, t) = u_i(\bar{x}, t^L; t^S) = u_i^L(\bar{x}, t^L) + u_i^S(\bar{x}, t^L; t^S). \tag{20}$$

Here, we assume that u_i^L does not depend on the SS time coordinate t^S, and is set to a constant in the t^S time scale. Thus, the time derivative in Eq. (19) is assumed to be with respect to t^S and the LS velocity field in Eq. (19) depends only on the spatial coordinates. To reduce computational expenses, while retaining two-way coupling between the LS and the SS, the SS Eq. (19) is solved on a collection of 1D lines embedded in domain Ω rather than in the whole domain Ω. Generally, there are no restriction on position of lines in Ω and their curvature. Here, for simplicity, we consider a family of lines $\Omega_l = \{l_1, l_2, l_3\}$ which consists of lines
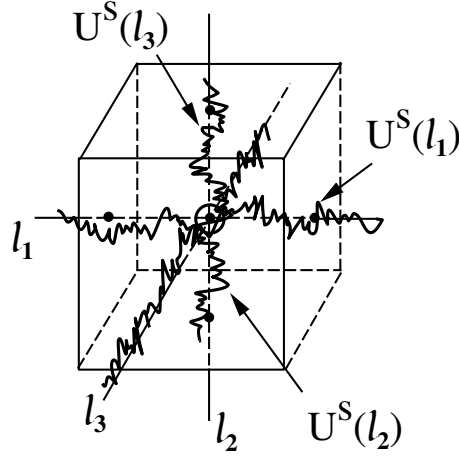
Figure 1. The SS 1D line arrangement within a 3D LS grid cell. One component of the SS velocity is shown on each line schematically.

parallel to corresponding LS coordinates $\{x_1, x_2, x_3\}$ and intersects each other at the LS grid nodes as shown in Figure 1, and introduce the SS fields defined on lines as: $u_i^S(\bar{x}, t^L; t^S) \longrightarrow u_{il_k}^S(l_k, t^L; t^S), \quad l_k \in \Omega$. Thus, in TLS we resolve the SS fields in the domain Ω_l only, while the LS fields are treated in Ω. Assume it is needed N_S^3 points to resolve the smallest dynamically important scales for DNS, and N_L^3 points to resolve only the large scale dynamics, as in LES. In respect of this resolution requirement, the TLS approach would fall in a category between DNS and LES, since it needs $N_L^3 + 3N_L^2 N_S$ points to represent both LS and SS fields. However, it is often the case for LES that N_L^3 has to be quite high ($N_L \to N_S$) in highly turbulent regions, for example near walls, to accurately predict the LS dynamics because of inherent limitations of the SGS models. In TLS, since the LS and SS are explicitly coupled, we expect less severe resolution requirements ($N_L^{TLS} < N_L^{LES}$) for the LS in highly turbulent regions. In addition, simulation of the SS fields on lines, which requires $3N_L^2 N_S$ point resolution, can be done in parallel reducing computational cost substantially.

Treating the SS fields on "less-dimensional" domain Ω_l is computationally more efficient, but there is a price to pay. When written on a line, say $l_1 = \{x_1, x_2 = C_2, x_3 = C_3\}$, where C_2, C_3 are constants, the SS equation (19) is not closed and requires knowledge of first derivatives of the SS velocity and pressure, and second derivatives of SS velocity in the directions l_2, l_3 which are orthogonal to the given line l_1. Thus, all derivatives of the SS fields in transversal directions to a given line have to be modeled, while all derivatives along the line can be computed as a part of solution. The second difficulty arise from the fact that at the LS grid nodes, where lines l_k intersect, the SS field becomes overdetermined since its values can be found from all three intersecting lines, and these values are not necessarily the same. Explicit requirement to have unique values of the SS fields at the LS grid points would lead to coupling of SS fields on different lines at those points, and therefore is not viable computationally. Instead, we decouple the SS field computations on lines, which means that the SS fields do not interact each other if they belong to different lines. The value of the SS field at the node $\{x_n\}$ of the LS grid G^Δ then defined as an average over all three lines intersecting at $\{x_n\}$:

$$u_i^S(x_n, t) \longleftarrow \left[u_{i,l_k}^S(x_n, t) \right]_{l_k}, \qquad x_n = \bigcap_{i=1}^{3} l_k, \quad k = 1, 2, 3 \tag{21}$$

One possible approach is to model unknown derivatives of the SS fields in terms of known ones by introducing functions f_j^i, g_j, h_j^i on each line l_k:

$$\frac{\partial u_i^S}{\partial x_j} = f_j^i \left(\frac{\partial u_i^S}{\partial x_k} \right), \quad \frac{\partial p^S}{\partial x_j} = g_j \left(\frac{\partial p^S}{\partial x_k} \right), \quad \frac{\partial^2 u_i^S}{\partial x_j^2} = h_j^i \left(\frac{\partial^2 u_i^S}{\partial x_k^2} \right), \tag{22}$$

$$i, j, k = 1, 2, 3 \quad j \neq k$$

These functions constitute the only model parameters under the current approach and have to be prescribed. Substituting these expressions together with the SS continuity equation into Eq. (19) gives the following

evolution equation for the SS velocity field on line l_k.

$$\frac{\partial u_i^S}{\partial t} + (u_j^L + u_j^S)\frac{\partial}{\partial x_j}(u_i^L + u_i^S \delta_{kj}) + (u_j^L + u_j^S)f_j^i(1 - \delta_{kj}) = \tag{23}$$

$$-\frac{\partial p^S}{\partial x_k}\delta_{ki} - g_i(1 - \delta_{ki}) + \nu\frac{\partial^2 u_i^S}{\partial x_k^2}\delta_{kj} + \nu h_j^i(1 - \delta_{kj}) + F_i^L(u_i^L, p^L)$$

$$i, j, k = 1, 2, 3$$

Before proceeding with analysis of the relationship between longitudinal and transverse derivatives of the SS fields, we first formulate the basic assumptions adopted here to solve Eq. (23).

(i) All first derivatives of the SS velocity in transverse directions to a given line l_k are much less than corresponding LS derivatives and neglected:

$$\frac{\partial u_i^S(l_k)}{\partial x_j} = 0 \quad i, j, k = 1, 2, 3 \quad j \neq k \tag{24}$$

(ii) All second derivatives of the SS velocity in transverse directions to a given line l_k are neglected:

$$\frac{\partial^2 u_i^S(l_k)}{\partial x_j^2} = 0, \quad i, j, k = 1, 2, 3 \quad j \neq k \tag{25}$$

(iii) Divergence-free requirement for the SS velocity field (18) is relaxed, as a result:

$$\frac{\partial p^S}{\partial x_j} = 0, \quad i, j, k = 1, 2, 3 \tag{26}$$

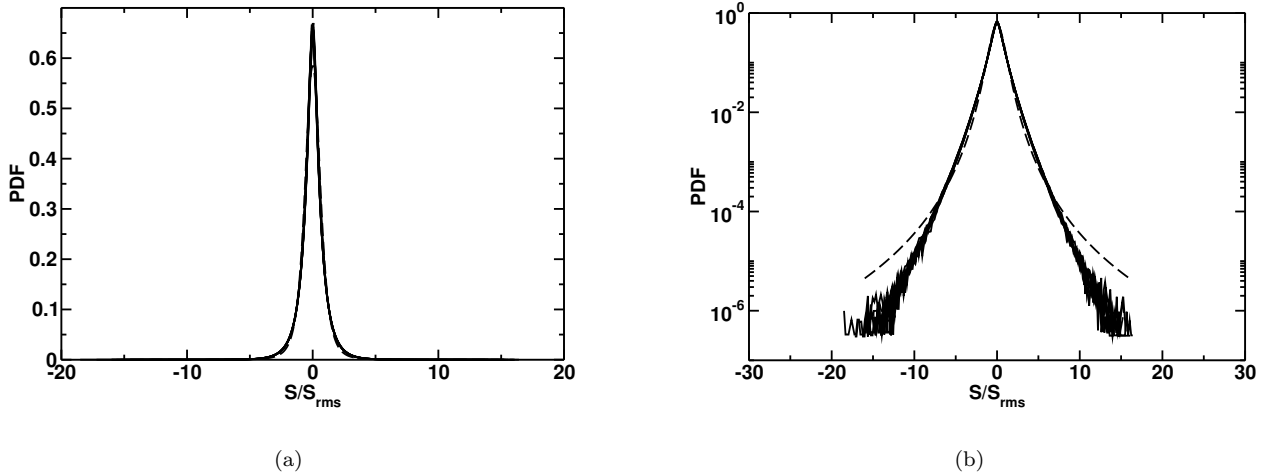(a)   (b)

Figure 2. PDF of the normalized differences of the first SS derivatives $S = \partial u_i^S / \partial x_j - \partial u_i^S / \partial x_k, j \neq k$ compared with the Tsallis distribution (dashed line): (a) in linear scale, (b) in logarithmic scale. Note that all nine PDFs are collapsed well.

There is a noticeable lack of comprehensive analysis of derivatives of the SS fields in literature, since most LES studies are concerned with modeling of the SGS stress, which represents the LS quantity. Here, to support (24), (25), and highlight the relationship between longitudinal and transverse derivatives of the SS fields, we use statistical analysis of isotropic turbulent 256^3 data set corresponding to $Re_\lambda = 116$ based on the Taylor micro-scale. The LS field is computed based on a uniform 32^3 LS grid using cubic spline interpolation, and then subtracted from the total field to obtain the SS field. Since for each velocity component, a derivative in line direction is always known, it is convenient to consider differences between derivatives in orthogonal directions.

Normalized PDFs of such differences $\partial u_i^S/\partial x_j - \partial u_i^S/\partial x_k$, $j \neq k$ are shown in Figures 2(a) and 2(b) in linear and logarithmic scale respectively. It is interesting to note they fit the Tsallis distribution quite well for wide range of probabilities. The Tsallis distribution was introduced in the context of turbulence by Beck.[6,7] It has a form $P_T(\xi) = 1/(Z_q[1 + (1/2)\beta(q-1)\xi^2]^{1/(q-1)})$ where Z_q is a normalization constant and $\beta = 2/(5-3q)$ is chosen to give a unit variance. It also reduces to a Gaussian distribution as $q \to 1$. Intuitively, it is clear from a representation of the SS field as a decomposition, that the SS derivatives should be relatively small everywhere except at the local high-gradient, turbulent regions. The most probable state of the SS velocity derivative differences is zero, suggesting that SS derivatives might be equal each other with high probability. However, this is not true, which is supported by Figures 3(a) and 3(b), which show scatter plots of the SS derivatives normalized by their rms (root-mean-square) values. These plots show correlations between longitudinal and transverse SS derivatives (Figure 3(a)), as well as, between two transverse SS derivatives (Figure 3(b)) of u_1^S component of the SS velocity. Other velocity components exhibit similar features. It is seen that the correlation between the SS derivatives is complex and nontrivial. Most probable

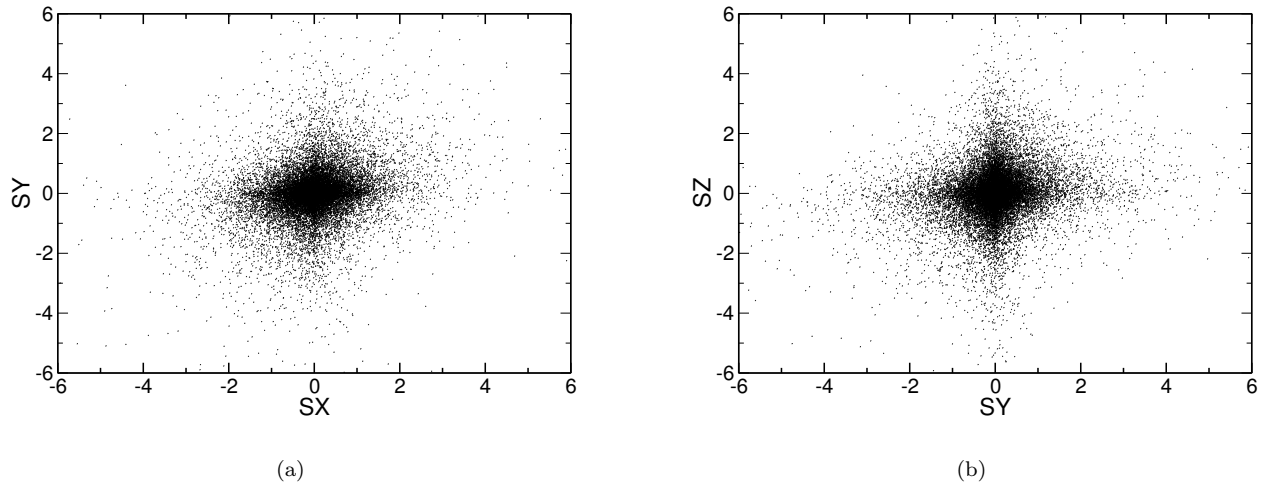(a)   (b)

Figure 3. Scatter plots of the normalized derivatives of the SS velocity: (a) longitudinal $\partial u_1^S/\partial x_1$ (SX) and transverse $\partial u_1^S/\partial x_2$ (SY); (b) transverse $\partial u_1^S/\partial x_2$ (SY) and transverse $\partial u_1^S/\partial x_3$ (SZ)

values of the SS derivatives are concentrated around the origin. The "star" shape of these scatter plots is clearly noticeable suggesting that events, when the SS derivatives are high in one direction and small in the orthogonal direction, and vice versa, might dominate the flow field, with exception of events when both derivatives are around origin and small.

It can be noted by inspection of the SS momentum Eq. (19) that first derivatives of the SS velocity enter the nonlinear term as a sum with the LS first derivatives. Scatter plots showing dependence between the LS derivatives and their sums with the SS derivatives are given in Figures 4(a) and 4(b) for the u_1 component of velocity. It is seen that the total derivatives is quite well correlated with the LS derivatives which makes the assumption given by Eq. (24) justifiable. Other velocity components produce similar behavior. Note that this assumption is only used in directions orthogonal to a line l_k, while the full sum of the LS and SS derivatives is retained along the line.

In a similar vein, second derivatives of the SS velocity can be analyzed. PDFs of differences between second derivatives of the SS fields are shown in Figures 5(a) and 5(b) and qualitatively exhibit the same features as differences of first derivatives. Again, the shape can be fairly well approximated by the Tsallis distribution for a wide range of probabilities. The scatter plots of longitudinal and transverse second order derivatives, normalized by their rms, are depicted in Figures 6(a) and 6(b) for the u_1^S velocity component. Other SS velocity components exhibit similar pattern and are not shown here for brevity. The "star" shape of these scatter plots follow the same shape as in case of first derivatives of the SS velocity, and resembles the astroid (hypocycloid with four cusps), a plane curve which is also shown in Figure 6(b). In parametric form, the astroid is given as $(x_1(t), x_2(t)) = (a\cos^3(t), a\sin^3(t))$, where a is parameter. This suggests a possible way to model unknown second derivatives in terms of the known ones in direction of line l_k. More specifically, we assume that for any point in space and time (x, t), and any velocity component, there is a

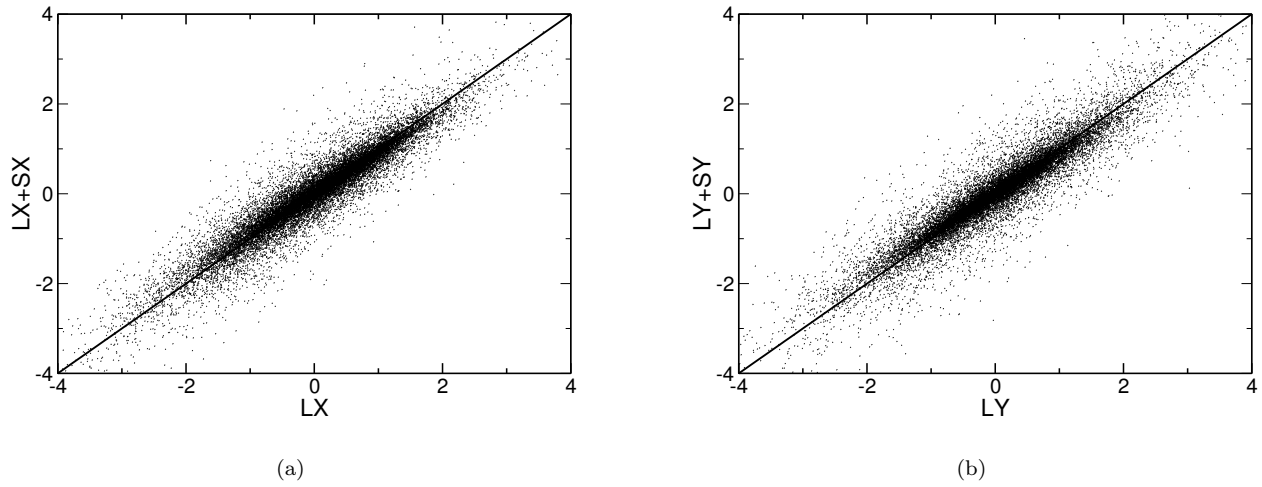(a)   (b)

Figure 4. Scatter plots of the normalized LS velocity derivative versus the total (LS+SS) velocity derivative: (a) longitudinal direction, $\partial u_1^L/\partial x_1$ (LX) and $\partial u_1^L/\partial x_1 + \partial u_1^S/\partial x_1$ (LX+SX); (b) transverse direction, $\partial u_1^L/\partial x_2$ (LY) and $\partial u_1^L/\partial x_2 + \partial u_1^S/\partial x_2$ (LY+SY). Straight line corresponds to a slope of one.
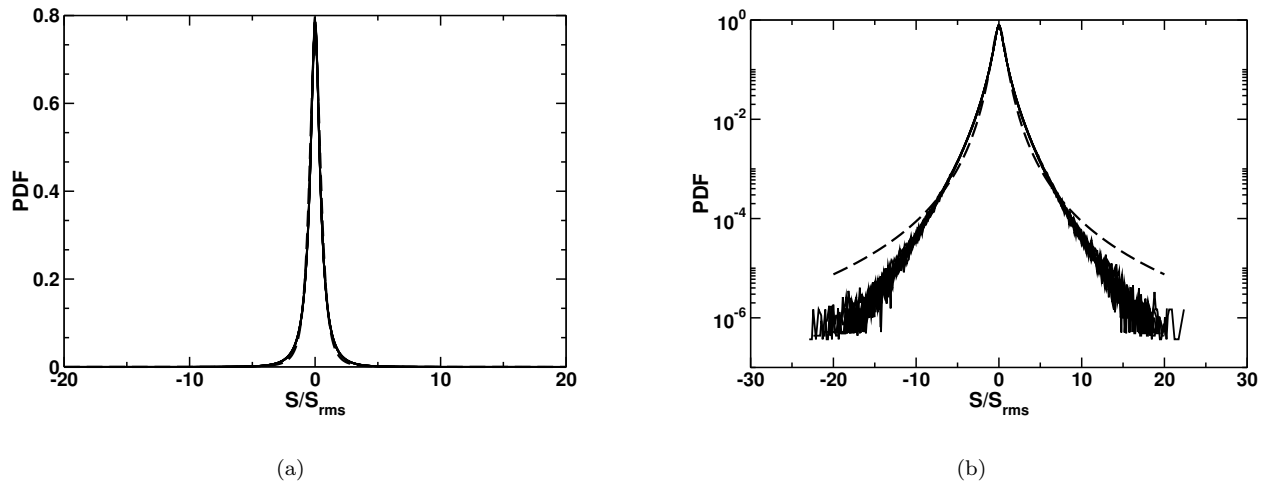

(a)   (b)

Figure 5. PDF of the normalized differences of the second SS derivatives, $S = \partial^2 u_i^S/\partial x_j^2 - \partial^2 u_i^S/\partial x_k^2, j \neq k$ compared with the Tsallis distribution (dashed line): (a) in linear scale, (b) in logarithmic scale. Note that all nine PDFs are collapsed well.

parameter a such that any pair of second derivatives of the SS velocity in orthogonal directions lie on the astroid with parameter a. Based on this assumption we compute PDF of the parameter a for all nine pairs of the second SS derivatives $(\partial^2 u_i^S / \partial x_k^2, \partial^2 u_i^S / \partial x_j^2), j \neq k$. The results are presented in Figures 7(a) and 7(b). It is seen that all PDFs of a collapse well and distributed log-normally, suggesting some universal behavior of this parameter.
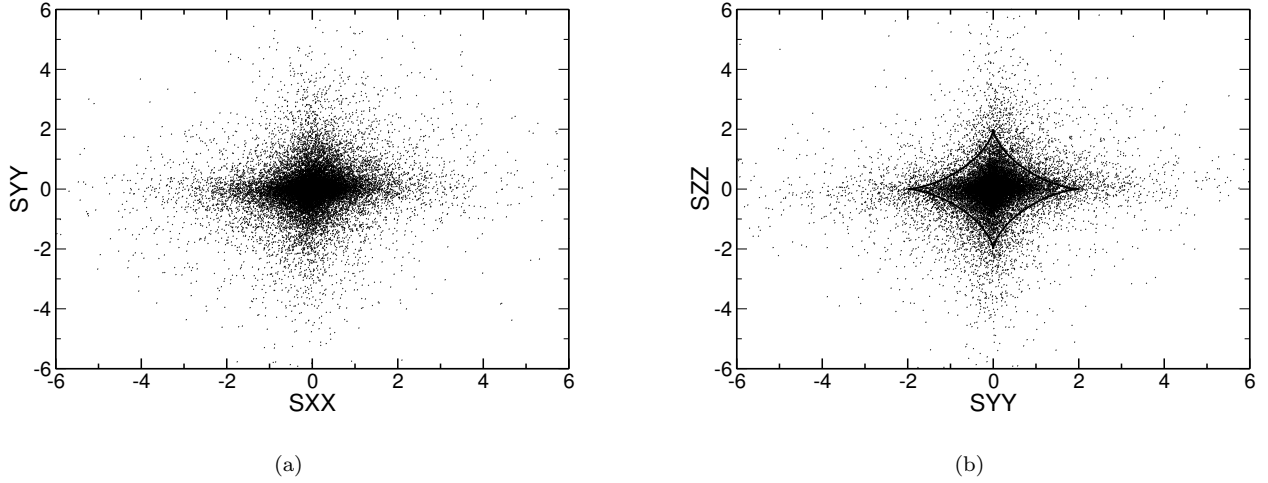

(a)   (b)

Figure 6. **Scatter plots of the normalized second derivatives of the SS velocity: (a) longitudinal $\partial^2 u_1^S / \partial x_1^2$ (SXX) and transverse $\partial^2 u_1^S / \partial x_2^2$ (SYY); (b) transverse $\partial^2 u_1^S / \partial x_2^2$ (SYY) and transverse $\partial^2 u_1^S / \partial x_3^2$ (SZZ). Solid line is the astroid curve with parameter $a = 2$.**

Therefore, a procedure for computing of unknown second derivative of the SS velocity results in sampling the parameter a from the log-normal distribution followed by the solution of the astroid equation based on the known value of the second derivative along the line l_k. Note that the same procedure can also be applied for estimation of the SS derivatives, instead of using the assumption (24), granted universal behavior of the parameter a. In this paper, similar to the assumption (24), we use the assumption given by Eq. (25) to model the unknown SS second derivatives. Clearly, for a given line l_k and velocity component u_i^S, if the second derivative along l_k is large in magnitude at some points then, as suggested by Figures 6(a) and 6(b), the second derivatives in the orthogonal directions are small with high probability. On the other hand, if the second derivative along l_k is small, then again, the corresponding second derivatives in orthogonal directions are small. Cases where the SS second derivative along l_k is small and the SS second derivative along orthogonal directions are large, happen with extremely low probability as follows from Figure 7.

Neglecting SS pressure gradient, according the assumption (26), means that the SS line velocity is divergence free. In principle, the unknown SS derivatives in continuity equation can be modeled according similar procedure as outlined above. However, since we are mostly interested in the LS dynamics here, the continuity requirement is only enforced on the LS. This is also consistent with the fractional step approach adopted for numerical simulation of the LS equations.

IV. Results and Discussion

In the numerical implementation of TLS approach, four steps are involved:

(i) At the n-th time step t_n^L, interpolate u_i^L and p^L onto each line l_k, such that: $u_i^L(\bar{x}, t^L) \longrightarrow u_{il_k}^L(l_k)$ and $p^L(\bar{x}, t^L) \longrightarrow p_{l_k}^L(l_k)$.

(ii) Solve Eqs. (23) on each line with corresponding boundary condition to obtain $u_{il_k}^S(l_k, t^S = t_n^L; t_n^L)$

(iii) Obtain the SS velocity u_i^S on the LS grid by averaging $u_{il_k}^S(l_k, t_n^L)$ over the three lines intersecting at the LS grid point x_n according to Eq. (21): $u_i^S(x_n, t_n^L) \longleftarrow u_{il_k}^S(l_k, t_n^L)$

(iv) Advance the LS velocity $u_i^L(\bar{x}, t_n^L)$ to time $t_{n+1}^L = t_n^L + \Delta t^L$ by solving Eq. (14). Here, Δt^L is the time step for evolving the LS field.
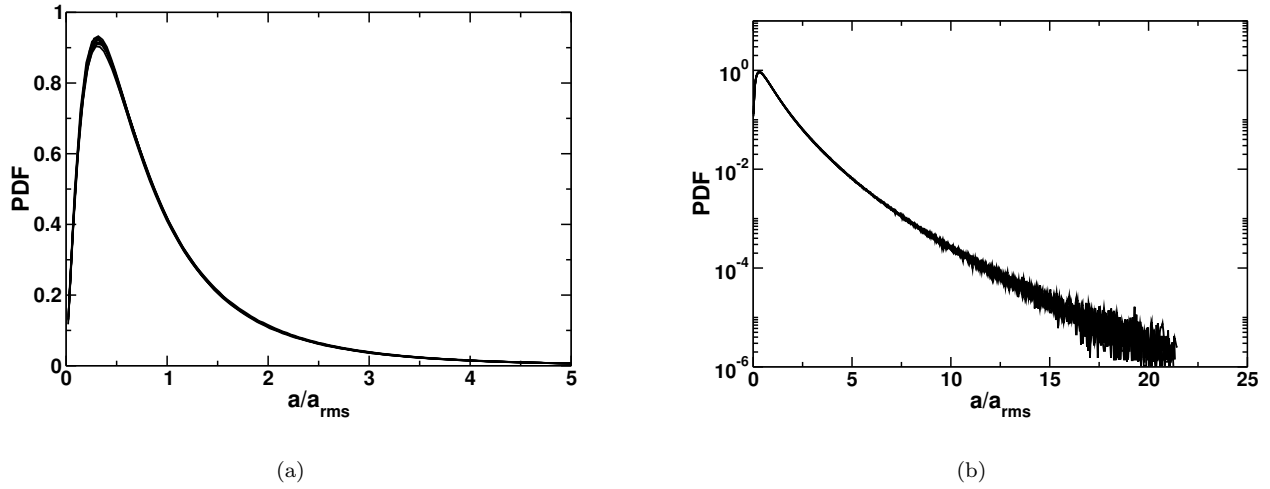
(a)

(b)

Figure 7. PDFs of the normalized parameter a/a_{rms} of the astroid for second derivatives of the SS velocity, $(\partial^2 u_i^S/\partial x_j^2)^{2/3} + (\partial^2 u_i^S/\partial x_k^2)^{2/3} = a^{2/3}, j \neq k$: (a) linear scale, (b) logarithmic scale. Note that all nine PDFs are collapsed well and fit the log-normal distribution.

Step (ii) solves a problem of reconstructing the SS velocity field $u_{il_k}^S$ along the line l_k, given the LS velocity field known. As a result, $u_{il_k}^S$ evolves from initial zero state, at a time step Δt^S, until the SS energy reaches the level of the LS energy at the smallest resolvable (cut-off) scale on the LS grid. This is illustrated in Figure 8, where evolution of the SS spectral energy and the SS velocity are shown for one line in isotropic turbulent field for three consecutive instants of time. Note that time t^S has meaning of the time needed for
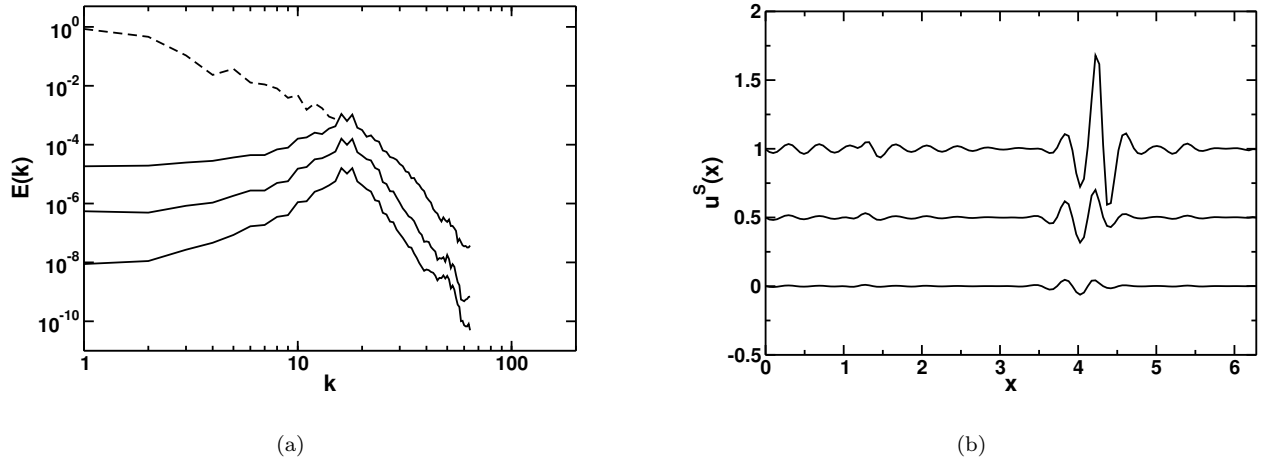

(a)

(b)

Figure 8. Evolution of the SS spectral energy (a) and the SS velocity (b) on a line for three consecutive instants of time t^S. The SS velocity is reconstructed when the LS (dashed line) and the SS (solid line) spectra are matched at the smallest LS (grid cut-off scale).

scale energy to propagate into the SS part of the spectrum. Due to nonlinear interactions between the LS and SS fields, the energy starts cascading down to the SS part of spectrum till it reaches the viscous cut-off level, thus creating the SS field. The evolution time needed to reconstruct SS velocity is different for various lines and fully defined by the LS field given on the line and viscosity. Typical LS and SS spectra for different lines in turbulent isotropic and channel flows are shown in Figures 9(a) and 9(b).

In step (iii), $u_{il_k}^S$ is averaged over three lines intersecting at the LS cell to obtain $u_i^S(x_n, t_n^L)$. This averaged u_i^S is considered the LS part of the SS velocity that is evolving at the slow time t^L on the LS grid. In step (iv), the LS field (Eq. 14) is forced by the LS part of the SS field in each cell. Further details on some early
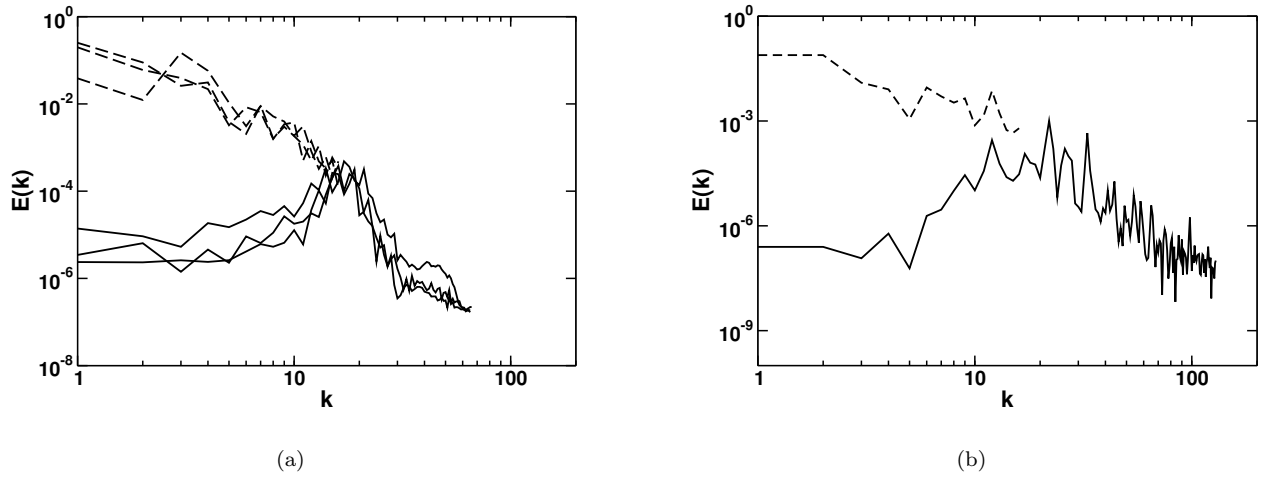
American Institute of Aeronautics and Astronautics Paper 2005-5318

(a)

(b)

Figure 9. The LS (dashed line) and the SS (solid line) energy spectra: (a) along three arbitrary lines in isotropic turbulence, (b) along a near-wall streamwise line in turbulent channel flow.

implementations of TLS approach can be found elsewhere.[8, 9]

A. Near-wall TLS for Channel Flow

Accurate modeling of the near-wall region constitutes the most difficult problem for LES. The maximum production of the turbulent kinetic energy occurs well within the inner layer at $y^+ \approx 12$ and shows very little variation with Reynolds number Re_τ. Very high near-wall resolution is needed to accurately predict turbulence generating events in the inner layer. Previous applications of the TLS method[10, 11] to simulate turbulent channel flow were focused on the whole flow domain including both inner and outer regions. They showed ability to capture near-wall flow behavior using grids coarser than needed by LES. However, overall cost reduction of TLS is only possible by effective handling of the SS field reconstruction. While
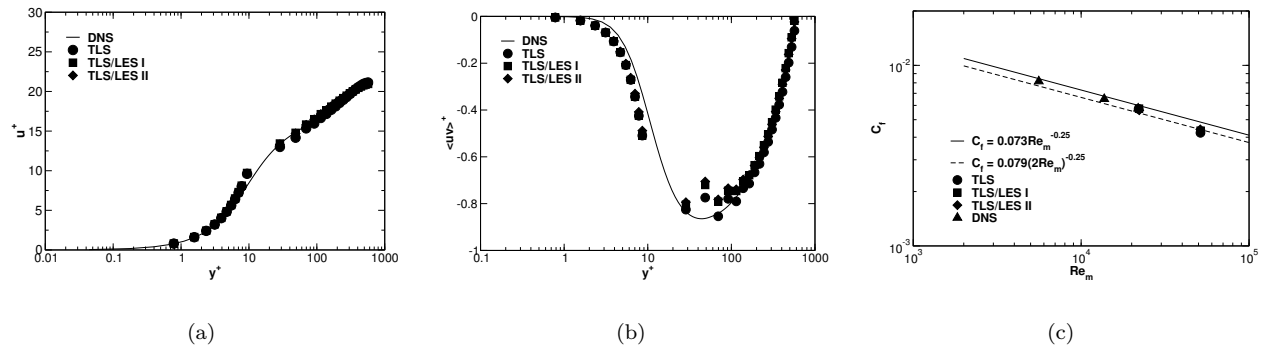

(a)

(b)

(c)

Figure 10. Combined TLS/LES compared to TLS and DNS calculations: (a) Mean velocity $\langle U^+ \rangle$; (b) Reynolds stress $\langle uv^+ \rangle$; (c) Friction coefficient C_f.

different strategies are available for parallelization of the SS line computations, applying TLS in the near-wall region only, together with LES in the outer region, results in drastic reduction in number of lines and can provide an interesting alternative to standard modeling approaches. In this effort we compare predictive capability of the combined TLS/LES methods with pure TLS calculations for turbulent channel flow at $Re_\tau = 590$. Near-wall regions are represented by three LS grid cells extending up to $y^+ \approx 50$ from walls. The standard LES with dynamic Germano subgrid model is used in the outer region. We consider two possible approaches to implement the combined TLS/LES calculations. In the first one, called TLS/LES-1, we use TLS calculations in the whole domain overwriting all outer region flow variables with that computed with LES. This implementation can not be considered as the "true" near-wall since computation of the SS

velocities on the wall normal lines is nonlocal and uses information from the outer flow region. However, it is still interesting to see how much the outer flow can affect the near-wall SS velocity fields. In the second
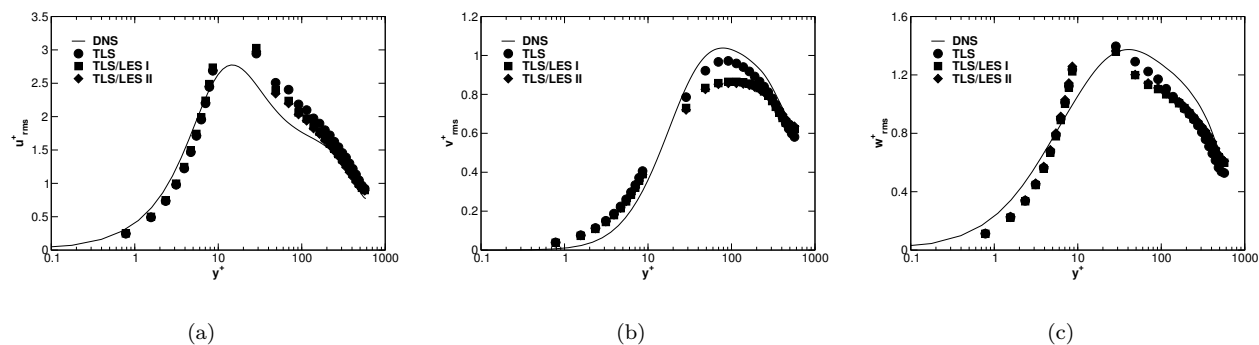

(a) (b) (c)

Figure 11. Combined TLS/LES compared to TLS and DNS calculations: (a) streamwise rms u'^+; (b) wall-normal rms v'^+; (c) spanwise rms w'^+.

approach, called TLS/LES-2, we consider two identical families of TLS lines (one for each wall) with short wall-normal lines. These wall-normal lines extends into three LS cells from the wall ($y^+ \approx 50$). Zero gradient boundary condition is used for all SS velocities at the "slip" end of the wall-normal lines. However, we point out that this boundary condition can be easily generalized to address real near-wall dynamics. Study of more physically plausible boundary conditions, where the SS velocities are represented by stochastic process with the mean proportional to local subgrid energy, is currently underway.

The statistical results of this study are shown in Figures 11 and 10. All TLS based calculations predict the near-wall region reasonably well. The combined TLS/LES calculations tend to underpredict rms fluctuations in the outer region compared to the pure TLS, except for the small core region (Figures 11(a-c)). This is due to more pronounced dissipation property of the Germano model. The Reynolds stress and the friction coefficient C_f are shown in Figures 10(b) and 10(c). Overall, the friction coefficient demonstrates the right trend slightly underpredicting the curve-fitted values of Dean.[12] Both combined TLS/LES approaches produce very close overall statistical results. Finally, high and low-speed streaks, shown in Figure 12 for TLS/LES-2 case, exhibit a typical near-wall pattern. This suggests that near-wall implementation of TLS may be viable alternative to LES of wall-bounded flows.
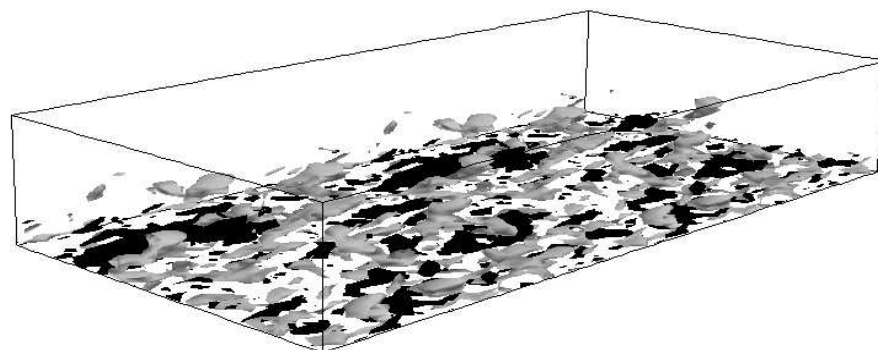

Figure 12. Isosurfaces of the streamwise velocity fluctuations: $u'^+ = +3$ (black) and $u'^+ = -3$ (gray).

B. TLS of Isotropic Turbulence

The TLS approach is also applied to simulate decaying and forced cases of homogeneous and isotropic turbulence. For the decaying case, a uniform 32^3 LS grid is used for 2π cubic domain. The SS velocity field is simulated on lines with uniform 256 point resolution. Initial LS velocity field was determined from a truncated developed 256^3 DNS turbulent field at $Re_\lambda = 116$. The objective of this simulation is to study

the response of the SS velocity to constantly diminishing LS velocity without mean flow. In the course of simulation the Taylor microscale Reynolds number is dropping from value of 116 to less than 60. Snapshots of the LS vorticity magnitude isosurfaces at a fixed level of $|\overline{\omega}^L| = 10.0$ are shown in Figures 13(a) and 13(c) for two consecutive instants of time $T = 0.75$ and $T = 3.0$. The corresponding isosurfaces of the resolved SS vorticity magnitude at a level of $|\overline{\omega}^S| = 0.14$ are shown in Figures 13(b) and 13(d). It is seen

(a)

(b)

(c)

(d)

Figure 13. Decay of isotropic turbulence: the LS (a, c) and the resolved SS (b, d) vorticity magnitude isosurfaces at the same intensity level for two instants of time $T = 0.75$ and 3.

that the LS vortical structures of high intensity gradually die out. The simulated SS field responds to the LS vorticity field in correct fashion by creating less intensive and more sparse SS vortical structures at later times. Further study is needed to compare decay rates of the LS and SS vortical structures.

The instantaneous line spectra of the LS and SS velocities for three different orthogonal lines are shown in Figure 9 (a). It is seen that the LS as well as the SS energy spectra do not show any directional dependence suggesting that TLS SS model is able to reproduce isotropic property at the SS line level. However, there is no smooth cut-off of the SS energy spectra at large wave numbers of the dissipation region, which may be
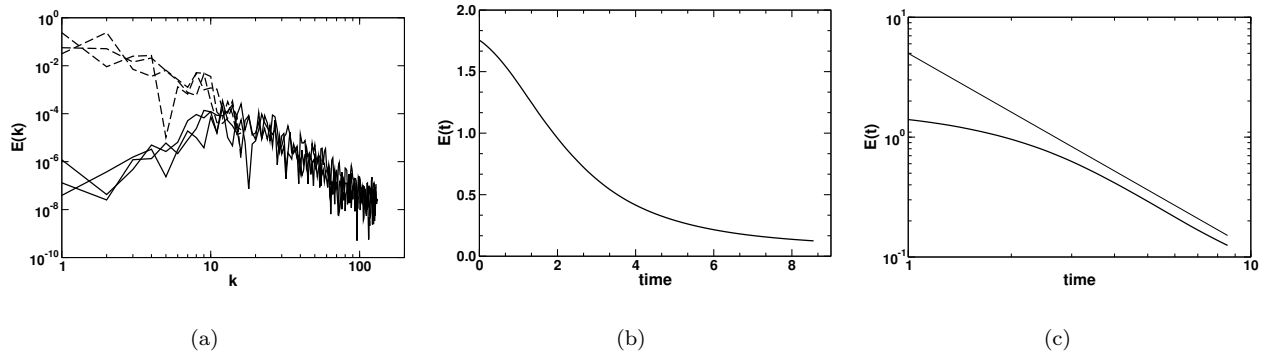
Figure 14. Decay of isotropic turbulence: (a) The LS (dashed line) and the SS (solid line) energy spectra along three orthogonal lines. The LS turbulent kinetic energy vs. time (b) in physical scale, (c) in logarithmic scale, the straight line corresponds to a slope of -1.5.

related to inadequate SS resolution. Overall the SS spectra are matched quite well with the LS spectra at the LS cut-off level which is important for correct reproduction of the SS influence on the LS. Decay of the LS turbulent kinetic energy is shown in Figures 14(a) and 14(b) and exhibits power-law behavior but with a little larger value of the decay exponent.

The forced isotropic turbulence presents the important ideal case to evaluate approximate turbulence modeling approaches. TLS of the forced isotropic turbulent flow has been conducted to study the ability of the model to sustain the stationary turbulent state at the LS and SS levels, and to provide an adequate energy coupling between the LS and SS. A matching DNS on 128^3 grid with the same forcing has also been performed to analyze the overall predictive capability of the TLS approach. A uniform 32^3 LS grid is used to discretize 2π cubic domain. All TLS lines have uniform 128 points resolution. For the chosen grid resolution, TLS code requires about an hour of CPU time on IBM SP4 to reach the stationary turbulent state, while it takes almost 17 hours of CPU time for DNS. Both codes were run in serial mode with the exception of the SS computation which was done in parallel using 48 processors.

Both simulations start with zero initial conditions and periodic in space. The force is concentrated around small wave numbers and gradually drives the flow to the stationary state. Here, we adopt the forcing scheme of Eswaran and Pope.[13] The random force of the form $\hat{f}_i(\mathbf{k}, t) = \delta_{ij} - k_i k_j / k^2 w_j(\mathbf{k}, t) \times [\Theta(\mathbf{k}) - \Theta(\mathbf{k} - \mathbf{k}_F)]$ is used, where $\mathbf{w}$ is Uhlenbeck-Ornstein stochastic process, δ_{ij} is the Kronecker delta and Θ is the Heaviside function. The process is of diffusion type, has zero mean and correlated over time with a chosen time scale τ. For a given grid resolution, three parameters define the intensity of forcing: the amplitude σ, the time-scale τ and the maximum wave number of the forced modes k_F. Here, we have taken the value of k_F, normalized by the lowest wavenumber, to be equal to $\sqrt{2}$. With the time scale $\tau = 0.95$ and the amplitude $\sigma = 0.04$, the forcing scheme produces the isotropic turbulent state with the Taylor microscale Reynolds number $Re_\lambda \approx 65$. However, as it was pointed out by Fureby $et\ al$[14] who used this method to study LES subgrid models, the same forcing can not be guaranteed for different grid resolutions. Nevertheless, we believe that is not a serious issue for comparison of TLS and DNS integral properties.

First of all, it is important to verify that TLS case is able to sustain the stationary turbulent state at the LS and SS levels and do not destroy isotropy of the flow. The evolution of the turbulent kinetic energies of the LS and the resolved SS is shown in Figure 15 (a). It is seen that both LS and SS reach the stationary state approximately at time $T \approx 8$. Note that the values of the resolved SS turbulent kinetic energy is multiplied by 5000 to make comparison possible. It is clearly seen that the SS energy is mimic the behavior of the LS energy suggesting the presence of the stationary energy cascade. The SS energy is also characterized by small intermittent high-frequency fluctuations. To gain a confidence that TLS calculation is, in fact, producing isotropic field, we compare the energy dissipation rate computed by the definition of $\epsilon = 2\nu s_{ij} s_{ij}$, where s_{ij} is the fluctuating strain rate, with the one computed based on the well-known isotropic formula $\epsilon_1 = 15\nu \langle (\partial u_1/\partial x_1)^2 \rangle$. Time evolution of these dissipation rates is depicted in Figure 15 (b).

In addition, the time evolution of individual rms velocity components along with the averaged rms-velocity scale are shown in Figure 16 (a). These figures suggest that TLS is able to capture the stationary isotropic state quite well. Figure 16(b) shows the averaged energy spectra of TLS and DNS cases after the
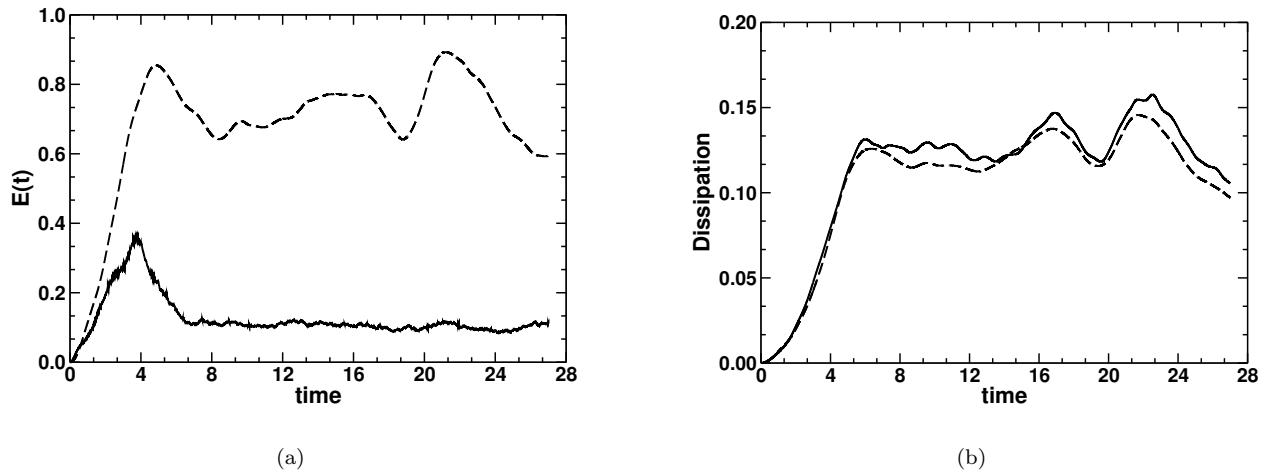
(a)

(b)

Figure 15. Forced isotropic turbulence: (a) Evolution of the turbulent kinetic energy of the LS (dashed line) and the resolved SS (solid line); (b) the LS dissipation rate ϵ^L (dashed line) and $\epsilon_1^L = 15\nu\langle(\partial u_1^L/\partial x_1)^2\rangle$ (solid line).

stationary state is reached. The TLS energy spectrum approximates the DNS spectrum quite satisfactorily, although it results in a small build-up of energy near the cut-off region. It can be related to the fact that
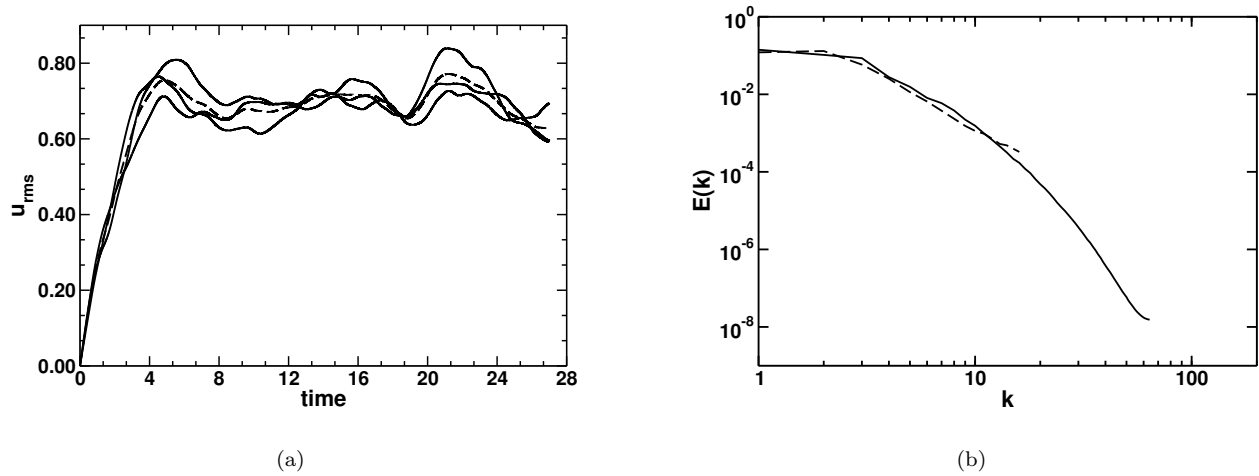

(a)

(b)

Figure 16. Forced isotropic turbulence: (a) Evolution of the LS rms velocities u_i' (solid line) and the LS rms-velocity scale v_{rms} (dashed line) for TLS; (b) the LS (dashed line) and DNS (solid line) energy spectra.

the SS evolution time has been chosen the same for all lines resulting in possible underestimation of the SS field on some particular lines. Note that in TLS approach, the SS fields are evolving from zero to the point when the LS and SS spectra are matched at the LS grid level. Generally, the SS time required to match spectra is different for different lines. Matching spectral condition is important to capture correct coupling between LS and SS fields. If the SS field grows too much it would produce unphysical effects on the LS field by backscattering extra energy at the LS grid level, eventually contaminating the LS field. On the other hand, if the SS field is not matched in spectral magnitude with the LS field at the LS grid level, it would not provide enough dissipation to the LS field causing the energy pile-up by blocking forward cascade. Further study is needed to rigorously address the issue of the SS evolution time, and its possible dependence on LS resolution and Reynolds number.

American Institute of Aeronautics and Astronautics Paper 2005-5318

V.   Conclusion

A novel approach to simulate high-Re flows has been developed based on the decomposition of velocity into large and small-scale components. A coupled system of large and small-scale equations that not closed based on an eddy-viscosity assumptions and require no adjustable parameters, has been derived and implemented to simulate turbulent channel flow and isotropic turbulence. A near-wall TLS combined with LES has been studied for the case of turbulent channel flow. Results suggest that the TLS approach has the potential for capturing turbulent flow behavior at high-Re using very coarse grids. More importantly, the closure assumption used in the TLS formulation has been shown to be reasonable based on application to different types of high-Re turbulent flows.

Acknowledgments

References

[1] Moser, R., Kim, J., and Mansour, N., "Direct numerical simulation of turbulent channel flow up to $Re_\tau = 590$," *Physics of Fluids*, Vol. 11, 1999, pp. 943–945.

[2] Piomelli, U. and Balaras, E., "Wall layer models for large eddy simulation," *Annual Review of Fluid Mechanics*, Vol. 34, 2002, pp. 349–374.

[3] Foias, C., Manley, O., and Temam, R., "Modeling on the interaction of small and large eddies in two-dimensional turbulent flows," *Mathematical Modeling and Numerical Analysis*, Vol. 22, 1988, pp. 93–114.

[4] Laval, J., Dubrule, B., and Nazarenko, S., "Dynamical modeling of sub-grid scales in 2D turbulence," *Physica D*, Vol. 142, 2000, pp. 231–253.

[5] Ghosal, S., "Mathematical and physical constraints on large eddy simulation of turbulence," *AIAA Journal*, Vol. 37, 1999, pp. 425–433.

[6] Beck, C., "Application of generalized thermostatistics to fully developed turbulence," *Physica A*, Vol. 277, 2000, pp. 115–123.

[7] Beck, C., "Superstatistics in hydrodynamic turbulence," *Physica D*, Vol. 193, 2004, pp. 195–207.

[8] Kemenov, K. and Menon, S., "A Two-Level Simulation Methodology for LES of High Reynolds Number Flows," *Advances in Turbulence IX*, CIMNE, 2002, pp. 203–206.

[9] Kemenov, K. and Menon, S., "Two level simulation of high-Re number non-homogeneous turbulent flows," *AIAA paper 2003-0084*, 2003.

[10] Kemenov, K. and Menon, S., "Two Level Simulation of High-Re Turbulent Flows," *Direct and Large-Eddy Simulation V, Proceedings of the fifth international ERCOFTAC workshop, Ercoftac Series*, Vol. 9, Kluwer, 2004, pp. 49–56.

[11] Fureby, C., Alin, N., Wikstrom, N., Menon, S., Svanstedt, N., and Persson, L., "Large-eddy simulation of high-Reynolds-number wall-bounded flows," *AIAA Journal*, Vol. 42, 2004, pp. 457–468.

[12] Dean, R. B., "Reynolds number dependence of skin friction and other bulk flow variables in two-dimensional rectangular duct flow," *Journal of Fluids Engineering*, Vol. 100, 1978, pp. 215–228.

[13] Eswaran, V. and Pope, S. B., "An examination of forcing in direct numerical simulations of turbulence," *Computers and Fluids*, Vol. 16, 1988, pp. 257–278.

[14] Fureby, C., Tabor, G., Weller, H. G., and Gosman, A. D., "A comparative study of subgrid scale models in homogeneous isotropic turbulence," *Physics of fluids*, Vol. 9, 1997, pp. 1416–1429.